MATERIALS SCIENCE

# Interfacial charge transfer and its impact on transport properties of $LaNiO_3/LaFeO_3$ superlattices

**Le Wang[1]*†, Zhifei Yang[2,3]†, Krishna Prasad Koirala[1], Mark E. Bowden[1], John W. Freeland[4], Peter V. Sushko[1], Cheng-Tai Kuo[5], Scott A. Chambers[1], Chongmin Wang[6], Bharat Jalan[2], Yingge Du[1]***



**Charge transfer or redistribution at oxide heterointerfaces is a critical phenomenon, often leading to remarkable properties such as two-dimensional electron gas and interfacial ferromagnetism. Despite studies on $LaNiO_3/LaFeO_3$ superlattices and heterostructures, the direction and magnitude of the charge transfer remain debated, with some suggesting no charge transfer due to the high stability of $Fe^{3+}$ ($3d^5$). Here, we synthesized a series of epitaxial $LaNiO_3/LaFeO_3$ superlattices and demonstrated partial (up to ~0.5 $e^-$/interface unit cell) charge transfer from Fe to Ni near the interface, supported by density functional theory simulations and spectroscopic evidence of changes in Ni and Fe oxidation states. The electron transfer from $LaFeO_3$ to $LaNiO_3$ and the subsequent rearrangement of the Fe 3d band create an unexpected metallic ground state within the $LaFeO_3$ layer, strongly influencing the in-plane transport properties across the superlattice. Moreover, we establish a direct correlation between interfacial charge transfer and in-plane electrical transport properties, providing insights for designing functional oxide heterostructures with emerging properties.**

## INTRODUCTION

$ABO_3$-type perovskite transition metal oxides (TMOs) exhibit numerous fascinating properties, including ferroelectricity, ferromagnetism, superconductivity, and adjustable electrical, optical, and catalytic functionalities, making them invaluable for diverse applications in electronics, energy conversion, and catalysis (*1*–*4*). Advances in thin-film growth methodologies, such as pulsed laser deposition and molecular beam epitaxy (MBE), synthesize junctions of two structurally similar but electronically distinct TMOs and form sharp heterointerfaces with atomic precision. These heterointerfaces often display exotic properties not observed in bulk materials due to the intricate interplay between charge, spin, orbital, and lattice order (*5*–*8*). Among various interfacial effects, charge transfer or redistribution is a common but important one, resulting in remarkable emergent properties, including two-dimensional (2D) electron gas and hole gas formation at the $LaAlO_3/SrTiO_3$ (STO) interface (*9*, *10*), exchange bias at the $LaMnO_3/LaNiO_3$ interface (*11*, *12*), interfacial ferromagnetism at the $SrMnO_3/SrIrO_3$ and $CaRuO_3/LaNiO_3$ interfaces (*13*, *14*), and unexpected magnetic anisotropy at the $La_{1-x}Sr_xMnO_3/SrIrO_3$ interface (*15*). Thus, understanding and controlling these charge transfer processes are essential for unlocking the full potential of oxide heterointerfaces in advanced technological applications.

Since the oxygen (O) sublattice is continuous across the interface, a simple electronic structural model in which the O 2p bands are aligned at the interface has been proposed to predict the direction and relative magnitude of interfacial charge transfer (*16*, *17*). According to this model, the energy difference between the O 2p band center ($\varepsilon_p$) and the Fermi level ($E_F$) of bulk components emerges as a critical parameter in determining the charge transfer dynamics (*17*). Specifically, electrons are expected to hop from compounds with more negative $\varepsilon_p$-$E_F$ to those with less negative $\varepsilon_p$-$E_F$. This prediction has been observed in various heterointerfaces involving 3d/3d and 3d/5d TMO systems, which typically share the same A-site element but feature different B-site elements, such as $LaTiO_3/LaFeO_3$ (LTO/LFO) (*18*, *19*), $LaTiO_3/LaCoO_3$ (*20*, *21*), $LaTiO_3/LaNiO_3$ (LTO/LNO) (*22*, *23*), $LaMnO_3/LaNiO_3$ (*11*, *24*–*26*), $SrVO_3/SrMnO_3$ (*27*), and $SrMnO_3/SrIrO_3$ (*13*, *28*). Moreover, the degree of charge transfer has been connected to the values of band offsets at the heterointerfaces (*17*). For example, nominally complete charge transfer from Ti to Ni has been demonstrated at the LTO/LNO interface due to the system exhibiting the largest band offset among all those involving first-row 3d TM elements at the B sites (*23*, *29*), leading to an emergent quasi-2D antiferromagnetic order with high magnetic exchange correlations (*30*). Similarly, electron transfer up to 1.2 ± 0.2 $e^-$/interface unit cell (u.c.) from Ti to Fe and the rearrangement of the Fe 3d bands have been observed at the LTO/LFO interface, resulting in a nonmagnetic band insulator interface phase (*18*).

In this work, we investigate charge transfer from Fe to Ni at the LNO/LFO interface. Bulk LNO is a paramagnetic metal, while bulk LFO is an antiferromagnetic charge transfer insulator. Compared to LTO/LNO and LTO/LFO systems, the LNO/LFO heterostructure exhibits a relatively smaller band offset (*16*, *17*). According to the O 2p band-alignment model (*17*), partial charge transfer from Fe to Ni is expected near the LNO/LFO interface. However, on the basis of the ionic bonding paradigm, no charge transfer should occur, as $Fe^{3+}$ in LFO is considered as a highly stable $3d^5$ system with a half-filled 3d orbital (*31*, *32*). Recent experimental studies support the latter model, where no such charge transfer was observed at the LNO/LFO heterostructures (*33*–*35*).

[1]Physical and Computational Sciences Directorate, Pacific Northwest National Laboratory, Richland, WA 99354, USA. [2]Department of Chemical Engineering and Materials Science, University of Minnesota–Twin Cities, Minneapolis, MN 55455, USA. [3]School of Physics and Astronomy, University of Minnesota–Twin Cities, Minneapolis, MN 55455, USA. [4]X-ray Science Division, Advanced Photon Source, Argonne National Laboratory, Lemont, IL 60439, USA. [5]Stanford Synchrotron Radiation Lightsource, SLAC National Accelerator Laboratory, Menlo Park, CA 94025, USA. [6]Environmental Molecular Sciences Laboratory, Pacific Northwest National Laboratory, Richland, WA 99354, USA.
*Corresponding author. Email: le.wang@pnnl.gov (L.W.); yingge.du@pnnl.gov (Y.D.)
†These authors contributed equally to this work.

Contrary to this, our previous study on $LaNi_{1-x}Fe_xO_3$ (LNFO) solid solutions showed that Fe substitution for Ni in LNO induced partial electron transfer from Fe to Ni sites, leading to oxidation states of $Ni^{3-\delta}$ and $Fe^{3+\delta}$ (*36*). The presence of $Fe^{3+\delta}$ cationic species in LNFO effectively increases the total TM 3d bandwidth via Ni–O–Fe bridges and enhances TM 3d-O 2p hybridization, thereby boosting the electrochemical activity. Unlike the random distribution of Fe in LNFO solid solutions, Fe is confined to LFO layers in LNO/LFO superlattices (SLs). Thus, determining the sign and magnitude of the charge transfer in these heterostructures is crucial for elucidating the impact of cation distribution near the surface on electronic states and related electrochemical properties.

Here, we present direct evidence of charge transfer from Fe to Ni at the LNO/LFO heterointerfaces. Our study integrates density functional theory (DFT) calculations with various spectroscopic techniques including in situ x-ray photoemission spectroscopy (XPS), ex situ x-ray absorption spectroscopy (XAS), and layer-resolved electron energy loss spectroscopy (EELS). Through these combined analyses, we conclude that electron transfer up to 0.5 $e^-$/interface u.c. from Fe to Ni occurs in these LNO/LFO SLs, as evidenced by spectroscopically determined changes in the Ni and Fe oxidation states within the $(LNO)_3/(LFO)_m$ SLs (where 3 and $m$ denote the number of u.c. for LNO and LFO, respectively). Furthermore, our analysis of the in-plane electrical transport data establishes a quantitative relationship between the magnitude of interfacial charge transfer and the corresponding changes in sheet resistance for $(LNO)_3/(LFO)_m$ SLs. These findings provide insights into the precise control of Ni and Fe oxidation states through heterointerface structural manipulation, which in turn hold substantial implications for designing and optimizing electronic and energy-related devices.

## RESULTS

### Interfacial charge transfer from Fe to Ni predicted by DFT

To theoretically model charge transfer at the LNO/LFO interface, we conducted DFT calculations on bulk LNO, bulk LFO, and an $(LNO)_3/(LFO)_1$ SL, all epitaxially strained to STO(001) substrates. A-type and G-type antiferromagnetic order was assumed for LNO and LFO, respectively (*18*, *37*, *38*). The calculated geometrical structure for the $(LNO)_3/(LFO)_1$ SL is illustrated in Fig. 1A. Figure 1B shows the density of states (DOS) projected onto atomic orbitals in layers containing $BO_2$ planes for bulk LNO (top), bulk LFO (bottom), and the $(LNO)_3/(LFO)_1$ SL (middle). Figure S1 displays the DOS projected in the O 2p, Fe s, p, $e_g$, and $t_{2g}$ orbitals, and Ni s, p, $e_g$, and $t_{2g}$ orbitals for bulk LFO and bulk LNO. Vertical black dash-dot lines and red dashed lines indicate the positions of $E_F$ and $\varepsilon_p$, respectively. Without introducing the Hubbard correction term ($U$), bulk LNO shows metallic behavior with nonzero Ni 3d DOS across $E_F$, consistent with experimental data. In contrast, bulk LFO exhibits a small gap, consistent with its insulating ground state. Analysis of the projected DOS (pDOS) allows us to generate the schematic band diagrams (Fig. 1C) and determine the energy difference between $\varepsilon_p$ and $E_F$ for bulk LFO and bulk LNO. Specifically, we find that the $\varepsilon_p$-$E_F$ values are −3.4 and −3.1 eV for bulk LFO and bulk LNO, respectively. This difference suggests that if we align the $\varepsilon_p$ values, as is customary due to the continuity of the O sublattice across the interface, the $E_F$ mismatch ($\Delta E_F$) between these two bulk phases is ~0.3 eV. Epitaxial strain, which strongly influences octahedral rotations in complex oxides

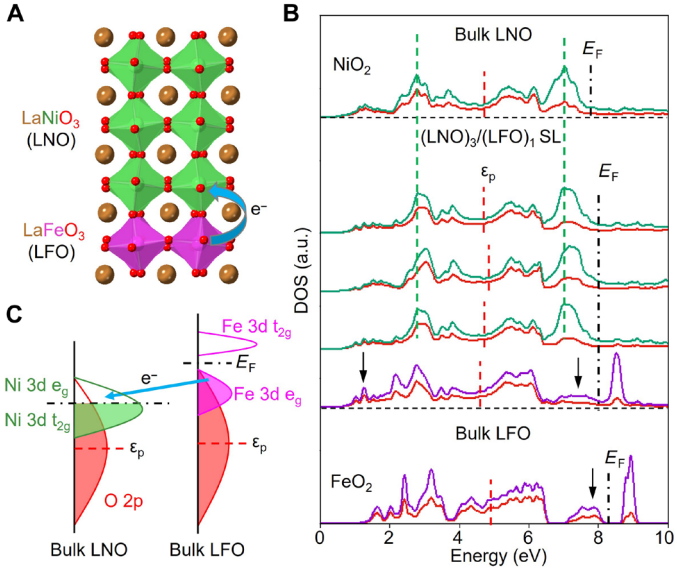


**Fig. 1. DFT calculation results.** (**A**) Side view of the optimized geometrical structure of the $(LNO)_3/(LFO)_m$ ($m = 1$) SL. (**B**) Calculated DOS projected on the $BO_2$ layers (green for $NiO_2$ and purple for $FeO_2$) and O 2p states (red lines) and the neighboring AO layers. The Fermi level ($E_F$) is labeled by a vertical black dash-dot line. The center of O 2p states ($\varepsilon_p$) is marked by a vertical red line. a.u., atomic unit. (**C**) Schematic of the energy bands before the formation of the LNO/LFO heterointerface. The blue arrows in (A) and (C) indicate the direction of interfacial charge (electron) transfer from Fe to Ni sites.

(*39*, *40*), can alter the orbital overlap and shift the energy levels (*41*–*43*), thereby affecting $\varepsilon_p$-$E_F$ values in both phase-pure LNO and LFO films as well as the $\Delta E_F$ value for LNO/LFO heterointerfaces. We observe that $\Delta E_F$ increases to ~0.6 eV when the substrate is changed from STO to $(LaAlO_3)_{0.3}(Sr_2AlTaO_6)_{0.7}$ (LSAT), which has a smaller lattice parameter than STO. This increase in $\Delta E_F$ is indicative of the impact of strain on the charge transfer across the heterointerface and the resulting in-plane transport properties of the SL. Since $E_F$ must be constant across heterostructures at equilibrium, we anticipate electron transfer from the occupied Fe 3d $e_g$-O 2p hybridized band to the unoccupied Ni 3d $e_g$-O 2p hybridized band (marked by the blue arrow in Fig. 1C) during the formation of the LNO/LFO heterostructure. This expectation is supported by our DFT findings for the $(LNO)_3/(LFO)_1$ SL. As seen in Fig. 1B, the top occupied Fe 3d $e_g$ bands in bulk LFO (marked by the black arrow at ~8 eV) are partially depleted in the $(LNO)_3/(LFO)_1$ SL. This electron depletion is accompanied by a downward shift of the $FeO_2$ layer pDOS relative to that of bulk LFO (marked by the black arrow at ~1.2 eV), suggesting an increase in the Fe formal charge in the SL. Furthermore, we observed an upward shift for all $NiO_2$ layer pDOS in the $(LNO)_3/(LFO)_1$ SL compared to bulk LNO, indicating that the Ni cation charge decreases relative to that in the bulk LNO and that the electron transfer occurs over all 3-u.c. LNO. These observations align with the scenario of charge transfer from LFO to LNO, consistent with the O 2p band-alignment procedure (*17*). Moreover, our DFT calculations reveal the presence of a metallic interfacial LFO layer (Fig. 1B) as a result of electron transfer from LFO to LNO and the subsequent rearrangement of the Fe 3d band. This finding indicates the formation of a new ground state within the LFO layer, which could have a notable impact on the in-plane transport properties of the SL—a topic we will discuss in detail later.

Moreover, Fig. 1B clearly indicates a high degree of hybridization between both Ni and Fe 3d orbitals and O 2p orbitals in the $BO_2$ layers within LNO and LFO, respectively. Thus, the actual charges on the Ni and Fe cations in bulk LNO and LFO are not the 3+ formal charge values generated by the ionic model (see fig. S2). The same is true for the SL according to Fig. 1B. However, we use the formal charge designations $3 + \delta$ and $3 - \delta$ throughout the discussion of charge transfer below as a convenience in our electron counting but not to designate the actual cationic charges.

### Synthesis and characterization of the $[(LNO)_3/(LFO)_m]_k$ SLs

To investigate charge transfer experimentally, we synthesized phase-pure 22-u.c.-thick LNO and 39-u.c.-thick LFO films, along with a series of $[(LNO)_3/(LFO)_m]_k$ SLs on (001)-oriented STO substrates using oxygen plasma–assisted MBE. Details of the growth are described in Materials and Methods. In situ reflection high-energy electron diffraction (RHEED) was used for real-time monitoring of film growth and surface structure/morphology. Figure 2A displays the growth sequence for $[(LNO)_3/(LFO)_m]_k$ SLs terminated with 3 u.c. of LNO, where $k$ was fixed at 6 and $m$ was varied from 1 to 8. RHEED patterns (fig. S3A) exhibit sharp, bright, and unmodulated streaks, revealing the epitaxial nature of the as-grown films with smooth surfaces. Atomic force microscopy (AFM) measurements (see the inset in Fig. 2B) further confirm the atomically smooth film surfaces with well-defined step terrace structures. In Fig. 2B, a representative x-ray reflectivity plot of the $m = 5$ SL reveals good agreement in the multilayer structure between experimental data and simulations, suggesting that the SLs maintain the targeted structures described in Fig. 2A. X-ray diffraction (XRD) patterns (fig. S3B) exhibit distinct Bragg peaks and thickness oscillation fringes, further indicating good crystallinity and planar morphology. Figure 2C shows XRD θ-2θ scans near the (003) reflection for all these samples. Reciprocal space mapping data (Fig. 2D) confirm that all as-grown samples were coherently strained to the STO substrate. The SL Bragg angle shifts to a lower 2θ value with increasing $m$, indicating an increase in the average out-of-plane lattice parameter ($c$) (Fig. 2E). As expected, the $c$ value for the $m = 8$ SL approaches that of the phase-pure LFO film.

### In situ XPS and ex situ XAS

To determine the B-site cation charges in these SLs, we conducted both in situ XPS and ex situ XAS measurements. XPS survey (fig. S4) revealed a substantial overlap between Ni 2p and La 3d features, as well as between Fe 2p and Ni LMM Auger peaks. Thus, Ni 3p and Fe 3p core-level spectra were used to determine changes in the formal charges of Ni and Fe in these SLs relative to those for films of the phase-pure materials. All spectra were shifted in energy, so the associated O 1s peaks fall at 530.0 eV. Figure 3A shows the Ni 3p spectra of the $(LNO)_3/(LFO)_m$ SLs, the phase-pure LNO ($Ni^{3+}$ reference) film, and a NiO ($Ni^{2+}$ reference) film (*44*). Compared to the $Ni^{3+}$ reference spectra, the lower Ni 3p binding energy observed for all $(LNO)_3/(LFO)_m$ SLs indicates a Ni formal charge less than 3+. In contrast, the Fe 3p peaks for all $(LNO)_3/(LFO)_m$ SLs shift toward higher binding energy relative to the phase-pure LFO ($Fe^{3+}$ reference) spectrum (Fig. 3B), indicating a Fe formal charge higher than 3+. Using nominal $Ni^{2+}$, $Ni^{3+}$, $Fe^{3+}$, and $Fe^{4+}$ reference data, we quantify the Ni and Fe formal charges by calculating the binding



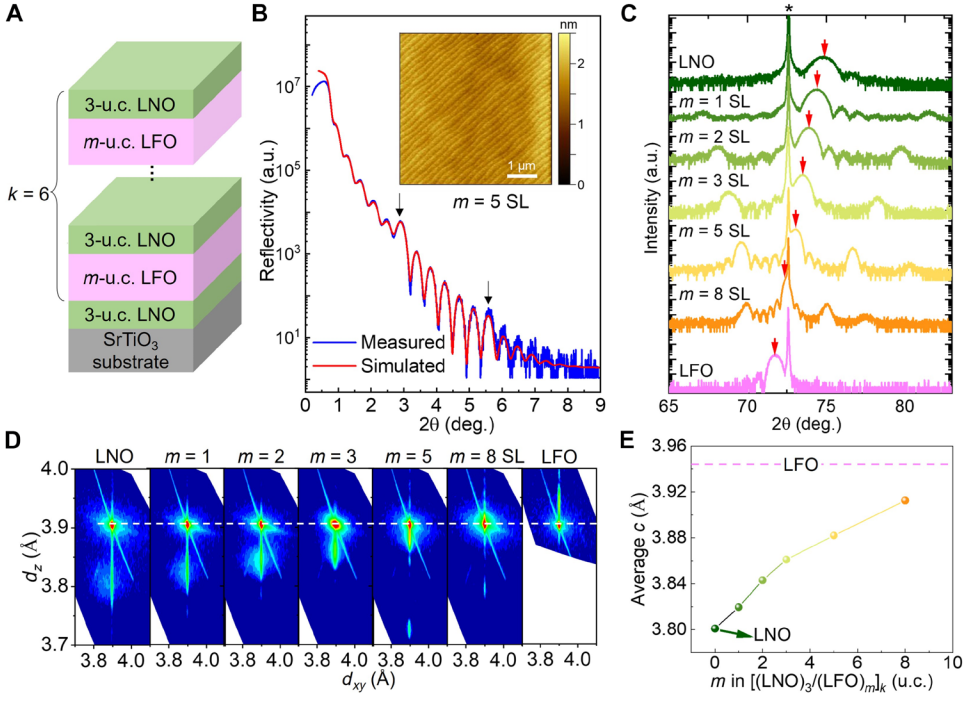


**Fig. 2. Synthesis and characterization of $[(LNO)_3/(LFO)_m]_k$ SLs.** (**A**) Schematic of the deposition sequence for these SLs. (**B**) X-ray reflectivity data and theoretical fit of an $m = 5$ SL, showing total thickness fringes as well as first- and second-order SL reflections (marked by black arrows). The inset displays a representative AFM image for the as-grown $m = 5$ SL on STO(001). The scan size is 5 μm by 5 μm. (**C**) Experimental XRD θ-2θ scans near the (003) reflection for the pure LNO film, $(LNO)_3/(LFO)_m$ SLs, and the pure LFO film. Red arrows indicate the main peaks for the SLs and films. "*" denotes the peak position of the STO substrate. (**D**) Reciprocal space maps near the (103) reflection of the substrate confirm coherent strain states. (**E**) Average out-of-plane lattice parameter ($c$) for the SLs as a function of $m$ (LFO layer thickness).

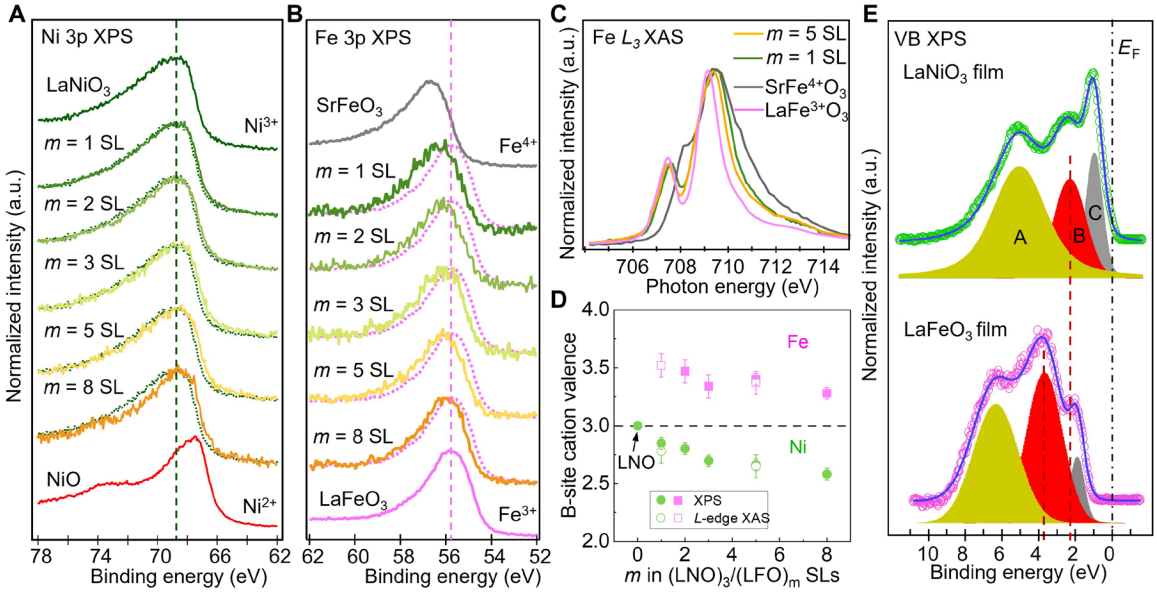


**Fig. 3. In situ XPS and ex situ XAS results.** The reference spectra for $Fe^{4+}$ and $Ni^{2+}$ were measured using oxygen plasma–annealed $SrFe^{4+}O_3$ and as-grown $Ni^{2+}O$ films, respectively. In situ Ni 3p (**A**) and Fe 3p (**B**) XPS. As a guide to the eye, we mark the Ni (Fe) 3p binding energy for the $LaNiO_3$ ($LaFeO_3$) film as a dashed green (purple) line. For comparison with SLs, we replot the Ni (Fe) 3p XPS spectra of the $LaNiO_3$ ($LaFeO_3$) film as dashed lines. (**C**) Fe $L_3$-edge XAS. (**D**) Spectroscopically determined B-site cation formal charges as a function of $m$ in $(LNO)_3/(LFO)_m$ SLs. Open (closed) squares are for Fe, and circles are for Ni and were taken from $L$-edge XAS (3p XPS). (**E**) VB XPS of the 22-u.c.-thick $LaNiO_3$ film grown on STO(001) and 39-u.c.-thick $LaFeO_3$ film grown on Nb-STO(001). The intensity was normalized to the area of the binding energy region of −2 to 10 eV. O 2p states (peaks A and B) and TM 3d states (peak C) are indicated schematically. Raw data are shown as open dots, while the fitting spectra are represented as blue lines. Dark red dashed lines denote the center of peak B. $E_F$ is labeled by a vertical black dash-dot line.

energy shifts in the Ni 3p and Fe 3p spectra (fig. S5) (*36*). The results are represented by closed circles (for Ni) and squares (for Fe) in Fig. 3D.

To assess $\varepsilon_p$-$E_F$ values experimentally, we examined the electronic structure of phase-pure LNO and LFO films in detail using valence band (VB) spectroscopy (Fig. 3E). The binding energy scale is accurate in an absolute sense, as no charging was observed during in situ XPS measurements. Both VB structures consist of bonding O 2p states (peak A), nonbonding O 2p states (peak B), and TM 3d states (peak C). After Shirley background subtraction, Voigt functions were used to fit the VB spectra. We determined the positions of the nonbonding O 2p states ($E_{O2p}$, relative to $E_F$) to be −3.7 eV for LFO and −2.3 eV for LNO, consistent with previous studies (*45*, *46*) and our DFT results shown in Fig. 1.

The formal charge changes determined using XPS were corroborated by XAS measurements collected in total fluorescence yield (TFY) mode at the Ni and Fe $L$-edges. Figure S6A compares the Ni $L_2$-edge spectra for the $(LNO)_3/(LFO)_m$ SLs with those of $Ni^{3+}$ and $Ni^{2+}$ reference materials. Notably, the shapes of the Ni $L_2$-edge spectra for the $(LNO)_3/(LFO)_m$ SLs deviate from that of the phase-pure LNO film, exhibiting a double-peak structure and suggesting a mix of $Ni^{2+}$ and $Ni^{3+}$ features in the SLs. Model spectra consisting of a linear combination of $Ni^{3+}$ and $Ni^{2+}$ reference spectra align well with the experimentally measured SL spectra (fig. S6A), facilitating the quantification of the average Ni formal charge in $(LNO)_3/(LFO)_m$ SLs. In addition, although the Fe $L_3$-edge spectra of $(LNO)_3/(LFO)_m$ SLs exhibit peak shapes similar to that of pure LFO, the broader Fe $L_3$-edge spectra (as shown in Fig. 3C) indicate a formal Fe charge greater than 3+ (*36*). To estimate the Fe formal charge in $(LNO)_3/(LFO)_m$ SLs, fitting based on linear combinations of $Fe^{3+}$ and $Fe^{4+}$ reference spectra was used. The resulting peak widths match the experimental data very well (fig. S6B). The formal charges deduced for Ni and Fe on the basis of Ni $L_2$-edge and Fe $L_3$-edge XAS spectra are also displayed in Fig. 3D as open circles (for Ni) and squares (for Fe). Together, our XPS and XAS measurements provide a consistent picture of electron transfer from Fe to Ni at the interface, resulting in the reduction of Ni formal charge and the increase in Fe formal charge in these $(LNO)_3/(LFO)_m$ SLs, in agreement with our DFT prediction (Fig. 1).

## Layer-resolved Fe oxidation states through EELS

Layer-resolved EELS was used to establish the spatial extent of electron transfer at the LNO/LFO interface. The left panel of Fig. 4A shows an atomically resolved, high-angle annular dark-field scanning transmission electron microscopy (HAADF-STEM) image of a representative $m = 5$ SL, viewed along the [100] direction. The right panel of Fig. 4A presents atomically resolved energy-dispersive spectroscopy maps, illustrating the elemental distributions of La (brown), Ni (green), Fe (purple), Sr (blue), and Ti (yellow) across the interface. A $TiO_2$-terminated STO surface is clearly visible at the film/substrate interface. Within the $m = 5$ SL, we observe limited Fe/Ni cation intermixing spanning ~1 u.c., as also confirmed in the $m = 1$ SL shown in fig. S7, comparable with findings from other epitaxial oxide interfaces (*47*–*50*). Because of the notable overlap between La $M$-edge and Ni $L$-edge EELS signals, our analysis primarily focuses on the Fe $L$-edge EELS results, which were conducted within an energy loss range of 690 to 740 eV, to examine variations in the Fe $L$-edge across the LNO/LFO interface. Fe $L_{2,3}$-edge EELS spectra measured at various locations (marked by black arrows in Fig. 4A) across the LNO/LFO interface are depicted with different colored lines in Fig. 4B. Compared to the phase-pure LFO film, the Fe $L_3$-edge EELS spectrum of the

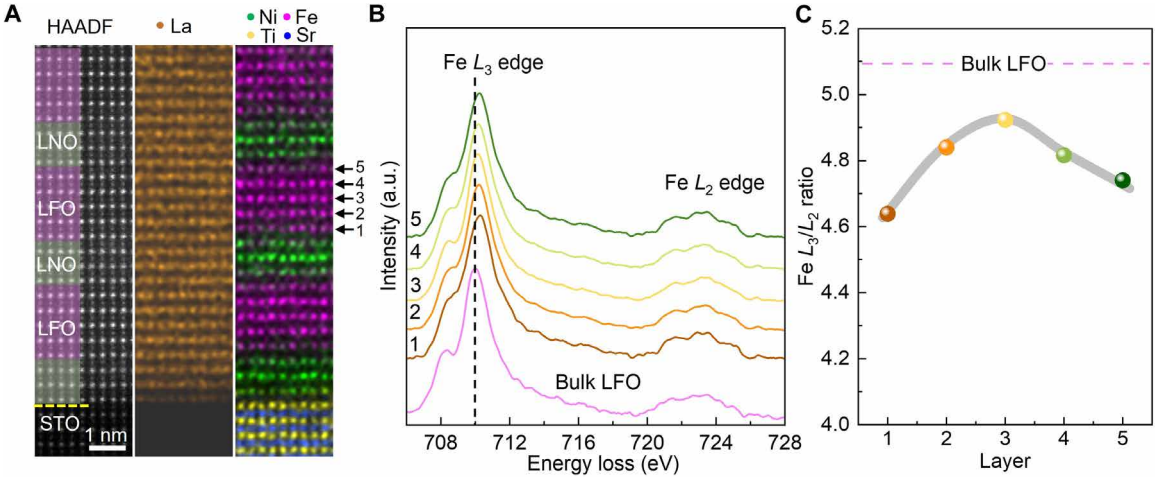


**Fig. 4. STEM-EELS results.** (**A**) HAADF-STEM image of the $m = 5$ SL and corresponding energy-dispersive spectroscopy maps. The black arrows point out which layer the corresponding EELS signal was taken from. (**B**) Layer-resolved EELS spectra of the Fe *L*-edge. The Ni *L*-edge spectra were not shown due to the strong overlap with the La $M_{4,5}$-edge. The black dashed line denotes the Fe $L_3$-edge peak position of bulk LFO. (**C**) Fe $L_3/L_2$ ratio as a function of each Fe layer in the $m = 5$ SL.

interfacial layers (layers 1 and 5) appears broader with a less well-resolved double-peak feature, suggesting that the Fe formal charge is higher than $Fe^{3+}$. Moreover, the observed energy shift (~0.3 eV) of the Fe $L_3$-edge relative to the phase-pure LFO also points to Fe in the interfacial layers having a formal charge higher than 3+. Looking next at the middle layer 3, the Fe $L_3$-edge displays a smaller energy shift and a clearer double-peak feature, indicating a lower Fe formal charge than is found in the interfacial LFO layers. Previous studies have demonstrated that the ratio of the integrated EELS intensities under the $L_3$- and $L_2$-edges can serve as a reliable indicator of the Fe valence (*19*, *51*, *52*). Typically, the $L_3/L_2$ ratio decreases with increasing formal charge from $Fe^{3+}$ to $Fe^{4+}$ (*52*), a trend also verified by our Fe *L*-edge XAS results for $LaFe^{3+}O_3$ and $SrFe^{4+}O_3$ reference materials (fig. S8). From the EELS data, we extract the Fe $L_3/L_2$ ratio for each LFO layer of the $m = 5$ SL. As summarized in Fig. 4C, the Fe $L_3/L_2$ ratio for each LFO layer was found to be smaller than that of pure LFO (~5.1), suggesting a formal charge higher than $Fe^{3+}$ for each LFO layer. In addition, the volcano shape of the $L_3/L_2$ ratios across 5-u.c. LFO indicates a decrease in Fe formal charge from the interface layer to the middle layer. Consequently, the Fe *L*-edge EELS results provide strong evidence of Fe oxidation from $Fe^{3+}$ in the bulk to a mixture of $Fe^{3+}$ and $Fe^{4+}$ at the interface. This indicates that electron transfer from Fe to Ni occurs at the LNO/LFO interface and spreads over at least 2 u.c., consistent with previously reported characteristic length (2 to 3 u.c.) of charge transfer at oxide heterostructures (*53*, *54*).

### Impact of charge transfer on in-plane electrical transport

To characterize the electrical properties of the SLs, we measured the sheet resistance ($R_S$) of the samples. As shown in Fig. 2A, the SL structure consists of seven layers of 3-u.c. LNO and six layers of *m*-u.c. LFO (where $m = 1$, 2, 3, 5, and 8). Considering the charge transfer at the LNO/LFO interface, the resistance contribution from each layer can be simplified as shown in Fig. 5A, where $R'_{LNO}$ represents the sheet resistance of 3-u.c. LNO after charge transfer, $R'_{LFO}$ denotes the sheet resistance of the *m*-u.c. LFO after charge transfer, and $R_{interface}$ represents the sheet resistance of the interfacial layer formed due to charge transfer from LFO to LNO. Note that $R'_{LNO}$ and $R'_{LFO}$ are, in principle, different from the intrinsic sheet resistance of 3-u.c. LNO and *m*-u.c. LFO, respectively, due to the charge transfer at the interface. Thus, the measured sheet resistance can be assumed to be the effective resistance of these individual layer sheet resistances in a parallel circuit. This simplified picture of resistance contribution can help us qualitatively understand the impact of interfacial charge transfer on transport behaviors.

Figure 5B presents the measured $R_S$ versus temperature ($R_S$-$T$) relationships for these SLs, along with the $R_S$-$T$ curve of the 22-u.c.-thick phase-pure LNO film (considered as the $m = 0$ case) for comparison. The sheet resistance was measured using the Van der Pauw geometry. As *m* increases, the sheet resistance of the samples also gradually increases. For *m* ranging from 0 to 5, the samples exhibit metallic behavior ($dR_S/dT > 0$) at high temperatures ($T > 200$ K). An upturn in $R_S$ as the temperature decreases is also observed with increasing *m*. The temperature at which the upturn occurs rises with increasing *m*, as illustrated by the arrows in fig. S9, which plots average resistivity (ρ) as a function of temperature using the total thickness of the SLs. This upturn could be attributed to the localization effect or the increasing contribution from intrinsic LFO layers as their thickness increases. For $m = 8$, the sample exhibits insulating-like behavior ($dR_S/dT < 0$), and the sheet resistance crosses the quantum resistance threshold ($h/e^2 \sim 25.8$ kilohms, where *h* is Planck's constant and *e* is the electron charge) at low temperatures. Furthermore, Hall measurements on both the 22-u.c. phase-pure LNO film and the SLs (fig. S10) indicate p-type conduction with holes as the majority carriers.

In Fig. 5C, we plot the measured conductance ($G = 1/R_S$) of the samples as a function of *m* at various temperatures. We define three regions in the plot (represented by a color gradient): small *m* ($m \leq 3$), large *m* ($m = 8$), and an intermediate range ($m = 5$). At first glance, *G* appears to decrease with increasing *m*, likely due to the increasing influence of the thicker intrinsic LFO layers. To quantitatively understand the contribution of each layer to the overall conductance, we use the analysis illustrated in Fig. 5A, where *G* can be characterized by the following formula

$$G = \frac{1}{R_S} = \frac{7}{R'_{LNO}} + \left(\frac{2}{R_{interface}} + \frac{1}{R'_{LFO}}\right) \times 6 \quad (1)$$

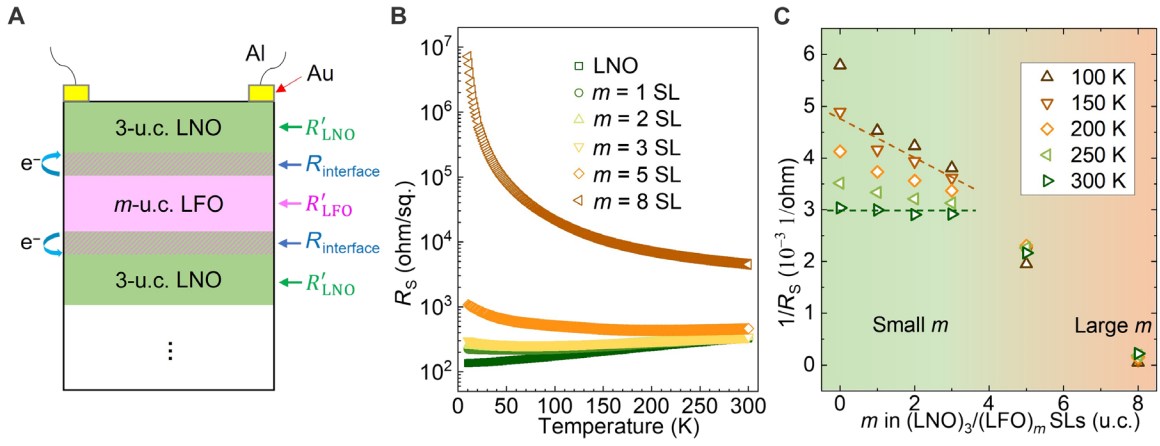


**Fig. 5. In-plane transport data.** (**A**) Proposed schematic of the SL structure with resistance contributions from different layers to the overall sheet resistance ($R_S$). (**B**) Measured $R_S$ as a function of temperature for $(LNO)_3/(LFO)_m$ SLs with varied $m$. Data of the 22-u.c.-thick phase-pure $LaNiO_3$ film (considered as $m = 0$) are also included for comparison. (**C**) Conductance ($1/R_S$) of $(LNO)_3/(LFO)_m$ SLs as a function of $m$ at different temperatures. Green and brown dashed lines are guides to illustrate the trends of $1/R_S$ with increasing $m$ at high temperatures and low temperatures, respectively.

Here, there are seven layers of 3-u.c. LNO with effective conductance $7 / R'_{LNO}$, six layers of $m$-u.c. LFO with effective conductance $6 / R'_{LFO}$, and 12 interfacial layers between LNO and LFO with effective conductance $12 / R_{interface}$. We assume that $R'_{LNO}$ and $R_{interface}$ remain constant across different SLs at a given temperature, while $R'_{LFO}$ varies with $m$. In the case of small $m$, the thermal energy available at ambient temperature drives hole hopping and overlapping of the interfacial layers, making the contribution of the intrinsic LFO layers to the overall conductance negligible. Hence, the SL conductance is effectively independent of the LFO layer thickness, as illustrated by the green dashed line in Fig. 5C. Such behavior can be captured using the following equation

$$G = \frac{1}{R_S} = \frac{7}{R'_{LNO}} + \frac{2}{R_{interface}} \times 6 \approx \frac{1}{R_{LNO}} \quad (2)$$

where $R_{LNO}$ is the measured sheet resistance of the 22-u.c. LNO film. In other words, when $m$ is small, it appears that only LNO layers contribute to the overall conductance. As verified from DFT calculations (Fig. 1) and layered-resolved Fe $L$-edge EELS results (Fig. 4), the charge transfer at the LFO/LNO interface spreads over at least 2 u.c. For the $(LNO)_3/(LFO)_m$ SL, there are two interfaces for each LFO layer with $m$-u.c. thickness. With $m \leq 3$, the interfacial layers can theoretically overlap and contribute to the conductance. Thus, the observation that the measured conductance is independent of $m$ when $m \leq 3$ at high temperatures indicates the presence of charge transfer at the LFO/LNO interface.

As the temperature decreases, carriers may start to localize because they lack enough thermal energy to overcome potential energy barriers between lattice sites. In addition, the width of the interfacial layer may decrease. Consequently, the influence of the intrinsic LFO layers on the overall conductance increases notably. On the basis of Eq. 1, at a given temperature, as the thickness of the LFO layer increases, $R'_{LFO}$ contributes more to the overall resistance, leading to a decrease in measured conductance. This trend is illustrated by the data at $T \leq 150$ K (guided by the brown dashed line) in Fig. 5C.

As $m$ increases to 5 and 8 u.c., the thickness of the LFO layer would eventually become larger than the width of the interfacial layer, and the properties of the intrinsic LFO layers progressively contribute to the overall measured conductance. According to Eq. 1, the increasing $R'_{LFO}$ from the LFO layer should not notably affect the measured conductance once $R'_{LFO}$ becomes at least one order of magnitude higher than the sheet resistance of other layers due to the resulting minimal value of $1 / R'_{LFO}$. However, since Al wires are connected to Au electrodes as illustrated in Fig. 5A and the wires are unlikely to penetrate throughout the entire SL to the STO substrate when the LFO layer is thick (*10*), what we are measuring is effectively

$$G = \frac{1}{R_S} = \frac{1}{R'_{LNO}} + \frac{1}{R_{interface}} + \frac{1}{R'_{LFO}} \quad (3)$$

This suggests that when LFO layers are thick, the measured conductance is likely dominated by the effective conductance of the top 3-u.c. LNO layer, the interfacial layer, and the first $m$-u.c. LFO layer, with reduced contributions from layers below. The thick LFO layer acts as an insulator and can potentially prevent the probe deep into the sample. Thus, the measured conductance decreases with increasing $m$ ($m \geq 5$). It has been demonstrated that LNO films exhibit a dimensionality-driven metal-to-insulator transition (*55*), where ultrathin LNO films (≤5 u.c.) show strongly localized character. With $m = 8$, we argue that the measurement primarily captures the behavior of 3-u.c. LNO, along with some contributions from the interfacial layer and 8-u.c. LFO. The measured sheet resistance shows an insulating-like behavior, consistent with the expected behavior of ultrathin LNO films. This observation provides an explanation for the low conductance of the $m = 8$ SL (Fig. 5C).

## DISCUSSION

In summary, we provide spectroscopic evidence based on two independent methods for electron transfer from Fe to Ni across interfaces with an LNO/LFO SL. The observed direction of electron transfer is consistent with our DFT calculations, which reveal that bulk LFO exhibits a more negative value of $\varepsilon_p$-$E_F$ compared to bulk LNO, consistent with the electron transfer criteria proposed in (*17*). The observation of change transfer from LFO to LNO is unexpected under the ionic bonding paradigm because in this model, $Fe^{3+}$ is taken to be a $d^5$ system and, as such, is thought to be unusually

stable (*31*–*33*). However, we emphasize that the high extent of hybridization between Fe 3d and O 2p orbitals that is evident from our DFT calculations shows that the electron count on Fe cations is not actually 5 but in fact greater than 5.

The character of the interfacial charge transfer is further supported by (i) our observations of a depleted Fe $e_g$–derived band and the downward shift of the $FeO_2$ layer pDOS relative to bulk LFO and (ii) the upward shift of the $NiO_2$ layer pDOS relative to bulk LNO in the $(LNO)_3/(LFO)_1$ SL. In addition, our DFT calculations reveal that this interfacial charge transfer, along with the depletion of Fe $e_g$–derived band, leads to the formation of a new metallic ground state within the LFO layers of the $(LNO)_3/(LFO)_1$ SL. By synthesizing a series of $(LNO)_3/(LFO)_m$ SLs with $m$ varying from 1 to 8 as a model system, we have created well-defined materials for analysis of the local electronic structure at the associated heterointerfaces. Our spectroscopic measurements for these $(LNO)_3/(LFO)_m$ SLs yield values for the changes in oxidation states for Ni and Fe, with the Ni charge dropping from $Ni^{3+}$ to $Ni^{3-\delta}$ and the Fe charge increasing from $Fe^{3+}$ to $Fe^{3+\delta}$. Quantitative analysis indicates electron transfer up to 0.5 $e^-$/interface u.c. from Fe to Ni in these LNO/LFO SLs. Layer-resolved Fe $L$-edge EELS data of a representative $(LNO)_3/(LFO)_5$ SL corroborate the direction of charge transfer, with the Fe charge at the interfacial layers surpassing that of the middle layer and both exhibiting higher oxidation states than bulk LFO.

Our analysis of in-plane electrical transport data establishes a direct link between the interfacial charge transfer and the measured sheet resistance of $(LNO)_3/(LFO)_m$ SLs. Our findings reveal that the interfacial charge transfer plays a substantial role in shaping the in-plane transport behavior, particularly in SLs with smaller LFO thickness ($m \leq 3$). In these cases, the charge transfer at the LNO/LFO interface results in an overlapping of the interfacial layers, which greatly affects the overall conductance. This is reflected in the independence of the measured conductance from LFO thickness at higher temperatures, as shown in Fig. 5C and explained through Eq. 2. The formation of a conductive interfacial layer due to charge transfer is further supported by our DFT calculations and layer-resolved Fe $L$-edge EELS results, which show that the charge transfer spreads over at least 2 u.c. at the interface, enabling overlapping contributions from adjacent interfacial regions.

Furthermore, as $m$ increases beyond 3, the transport properties become progressively dominated by the thicker LFO layers, especially at lower temperatures. For example, the insulating-like behavior for the $m = 8$ SL sample illustrates the point where the intrinsic LFO layers notably affect the transport characteristics, although charge transfer still plays a role at the interface. The transition from metallic to insulating-like behavior with increasing LFO thickness underscores the combined influence of both the intrinsic LFO layers and the charge transfer on the overall transport characteristics. In addition, our DFT calculations reveal that using a more compressively strained substrate, relative to bulk LFO, can lead to the increase in $\Delta E_F$ at the LNO/LFO interfaces. This change can strongly influence the extent of charge transfer and, consequently, the in-plane transport properties of the LNO/LFO SLs. These findings underscore the pivotal role of interface engineering in tailoring the electronic properties of complex oxides. Overall, this work represents a notable step forward in our endeavor to harness the potential of oxide heterostructures for next-generation electronic and energy-related technologies because it provides fundamental insights into the interplay between structure, charge transfer, and electronic properties.

## MATERIALS AND METHODS

### Sample growth

All $(LNO)_3/(LFO)_m$ SLs and pure LNO and LFO thin films were fabricated on (001)-oriented undoped $TiO_2$-terminated STO or 0.5 wt % Nb-doped STO (Nb-STO) substrates using oxygen plasma–assisted MBE. La, Ni, and Fe were evaporated from high-temperature effusion cells, and their individual evaporation rates were calibrated using a quartz crystal oscillator before each growth. The substrate temperature was maintained at 650°C, while the activated oxygen partial pressure remained at ~$3 \times 10^{-6}$ torr throughout the growth process. In situ RHEED served to monitor the overall growth rate and surface crystallography and structure. Sequential assembly of SLs with varying LNO and LFO layer thicknesses was achieved through shutter-controlled deposition. After growth, the sample was gradually cooled down to room temperature at a rate of 25°C/min under an activated oxygen atmosphere. The choice of a 22-u.c. thickness for the LNO film allows for a meaningful comparison to the $(LNO)_3/(LFO)_m$ SL (comprised of seven layers of 3-u.c. LNO and six layers of $m$-u.c. LFO), which contains a total of 21 u.c. of LNO. For the pure LFO thin film, we chose a thickness of 39 u.c. to ensure that the VB XPS signals accurately reflect the bulk LFO, minimizing any potential influence from the LFO/Nb-STO interface (*56*).

### XPS and XAS measurements

In situ XPS measurements were conducted on all freshly grown samples. A low-energy electron flood gun was used to neutralize the surface charge. The binding energy scale of Ni 3p and Fe 3p XPS spectra was calibrated by using the O 1s binding energy as an internal reference and set to 530.0 eV for all samples. TFY mode XAS measurements of the Fe and Ni $L$-edges were carried out at the beamline 4-ID-C of the Advanced Photon Source. In addition, total electron yield mode Fe and Ni $L$-edge XAS measurements of select samples were also carried out at the beamline 13-3 of the Stanford Synchrotron Radiation Lightsource to verify the formal charge changes in Fe and Ni. The total electron yield XAS results aligned with those obtained from TFY measurements, indicating similar trends in the changes of charge states for both Fe and Ni. All XPS and XAS measurements were conducted at 300 K, with x-rays incident at a normal angle to the sample surface.

### Sample characterization

The surface morphology of all samples was characterized by AFM (Dimension Icon), while their lattice structures were analyzed using a high-resolution x-ray diffractometer (Rigaku SmartLab). The cross-sectional STEM specimens were prepared using focused ion beam (FIB) techniques. Specifically, a FEI Helios Hydra FIB-SEM with a Xe plasma source from Thermo Fisher Scientific was used. The FIB was operated within a voltage range from 30 kV down to 2 kV to extract a cross-sectional lamella for the TEM sample. Initially, the lamella was thinned to approximately 200 nm at 30 kV, followed by additional milling steps at 5 and 2 kV, with the final milling step carried out at 2 kV to reduce the thickness to around 50 nm. For the STEM experiments, a Spectra-Ultra microscope equipped with an aberration corrector and field emission gun was used. The semiconvergence angle was set to 30 mrad, and the semicollection angle range was set to 60 to 200 mrad for HAADF-STEM imaging. Both HAADF imaging and EELS were conducted at an acceleration voltage of 300 kV and a probe current of approximately 30 pA. The STEM-EELS data were collected using a Gatan Imaging Filter Quantum spectrometer

(Gatan Inc.) with a low dispersion of 0.05 eV/channel to an active energy resolution of ~400 meV for analyzing the Fe and La *L*-edges. Calibration of the energy scale was achieved by acquiring spectra in dual-EELS mode, which simultaneously captures the zero-loss spectrum along with the Fe and La *L*-edge spectra.

### In-plane electrical transport measurements

To make ohmic contact, 30-nm-thick Au films were deposited on four corners of the as-grown samples using sputtering. Van der Pauw geometry was used for both electrical transport and Hall measurements, with Al wire–bonded contacts connecting to the Au electrodes. These measurements were carried out using a 9 T Quantum Design DynaCool physical property measurement system, with temperatures ranging from 10 to 300 K and a warming rate of 3 K/min.

### DFT calculations

Bulk LNO, bulk LFO, and the $(LNO)_3/(LFO)_1$ SL configurations were represented using the 2 by 2 by 4 supercells and strained to the STO(001) and LSAT(001) substrate. In all cases, the off-interface lattice parameters were adjusted to minimize the total energies of the corresponding systems. The calculations used the PBEsol exchange-correlation functional (*57*) within the Vienna Ab initio Simulation Package (*58*) using projector augmented-wave potentials to approximate the electron-ion interactions (*59*). A 500-eV plane-wave basis was used, with a 4 by 4 by 2 gamma-centered *k*-mesh for energy minimization and 8 by 8 by 4 *k*-mesh for DOS calculations. The total energy convergence criterion was set to $10^{-5}$ eV. One-electron DOS was smeared by convoluting it with Gaussian functions with a full width at half maximum of 0.1 eV for both valence and conduction band states.

## Supplementary Materials

**This PDF file includes:**

Figs. S1 to S10

References

## REFERENCES AND NOTES


1. R. E. Cohen, Origin of ferroelectricity in perovskite oxides. *Nature* **358**, 136–138 (1992).
2. J. Hwang, R. R. Rao, L. Giordano, Y. Katayama, Y. Yu, Y. Shao-Horn, Perovskites in catalysis and electrocatalysis. *Science* **358**, 751–756 (2017).
3. C. Sun, J. A. Alonso, J. Bian, Recent advances in perovskite-type oxides for energy conversion and storage applications. *Adv. Energy Mater.* **11**, 2000459 (2021).
4. J. Sunarso, S. S. Hashim, N. Zhu, W. Zhou, Perovskite oxides applications in high temperature oxygen separation, solid oxide fuel cell and membrane reactor: A review. *Prog. Energy Combust. Sci.* **61**, 57–77 (2017).
5. P. Zubko, S. Gariglio, M. Gabay, P. Ghosez, J.-M. Triscone, Interface physics in complex oxide heterostructures. *Annu. Rev. Condens. Matter Phys.* **2**, 141–165 (2011).
6. H. Y. Hwang, Y. Iwasa, M. Kawasaki, B. Keimer, N. Nagaosa, Y. Tokura, Emergent phenomena at oxide interfaces. *Nat. Mater.* **11**, 103–113 (2012).
7. R. Ramesh, D. G. Schlom, Creating emergent phenomena in oxide superlattices. *Nat. Rev. Mater.* **4**, 257–268 (2019).
8. L. Wang, Z. Yang, M. E. Bowden, J. W. Freeland, P. V. Sushko, S. R. Spurgeon, B. Matthews, W. S. Samarakoon, H. Zhou, Z. Feng, M. H. Engelhard, Y. Du, S. A. Chambers, Hole-trapping-induced stabilization of $Ni^{4+}$ in $SrNiO_3/LaFeO_3$ superlattices. *Adv. Mater.* **32**, e2005003 (2020).
9. A. Ohtomo, H. Hwang, A high-mobility electron gas at the $LaAlO_3/SrTiO_3$ heterointerface. *Nature* **427**, 423–426 (2004).
10. H. Lee, N. Campbell, J. Lee, T. J. Asel, T. R. Paudel, H. Zhou, J. W. Lee, B. Noesges, J. Seo, B. Park, L. J. Brillson, S. H. Oh, E. Y. Tsymbal, M. S. Rzchowski, C. B. Eom, Direct observation of a two-dimensional hole gas at oxide interfaces. *Nat. Mater.* **17**, 231–236 (2018).
11. M. Gibert, P. Zubko, R. Scherwitzl, J. Íñiguez, J.-M. Triscone, Exchange bias in $LaNiO_3$–$LaMnO_3$ superlattices. *Nat. Mater.* **11**, 195–198 (2012).
12. M. Gibert, M. Viret, P. Zubko, N. Jaouen, J.-M. Tonnerre, A. Torres-Pardo, S. Catalano, A. Gloter, O. Stéphan, J.-M. Triscone, Interlayer coupling through a dimensionality-induced magnetic state. *Nat. Commun.* **7**, 11227 (2016).
13. J. Nichols, X. Gao, S. Lee, T. L. Meyer, J. W. Freeland, V. Lauter, D. Yi, J. Liu, D. Haskel, J. R. Petrie, E.-J. Guo, A. Herklotz, D. Lee, T. Z. Ward, G. Eres, M. R. Fitzsimmons, H. N. Lee, Emerging magnetism and anomalous Hall effect in iridate–Manganite heterostructures. *Nat. Commun.* **7**, 12721 (2016).
14. J. Zheng, W. Shi, Z. Li, J. Zhang, C.-Y. Yang, Z. Zhu, M. Wang, J. Zhang, F. Han, H. Zhang, Y. Chen, F. Hu, B. Shen, Y. Chen, J. Sun, Charge-transfer-induced interfacial ferromagnetism in ferromagnet-free oxide heterostructures. *ACS Nano* **18**, 9232–9241 (2024).
15. D. Yi, J. Liu, S.-L. Hsu, L. Zhang, Y. Choi, J.-W. Kim, Z. Chen, J. D. Clarkson, C. R. Serrao, E. Arenholz, P. J. Ryan, H. Xu, R. J. Birgeneau, R. Ramesh, Atomic-scale control of magnetic anisotropy via novel spin–orbit coupling effect in $La_{2/3}Sr_{1/3}MnO_3/SrIrO_3$ superlattices. *PNAS* **113**, 6397–6402 (2016).
16. H. Chen, A. Millis, Charge transfer driven emergent phenomena in oxide heterostructures. *J. Phys. Condens. Matter* **29**, 243001 (2017).
17. Z. Zhong, P. Hansmann, Band alignment and charge transfer in complex oxide interfaces. *Phys. Rev. X* **7**, 011023 (2017).
18. J. E. Kleibeuker, Z. Zhong, H. Nishikawa, J. Gabel, A. Müller, F. Pfaff, M. Sing, K. Held, R. Claessen, G. Koster, G. Rijnders, Electronic reconstruction at the isopolar $LaTiO_3/LaFeO_3$ interface: An X-ray photoemission and density-functional theory study. *Phys. Rev. Lett.* **113**, 237402 (2014).
19. C. Gu, M. Gu, C. Zhang, Z. Yuan, Z. Gu, J. Zhou, Y. Nie, P. Wang, X. Pan, Atomic-resolution study of charge transfer effects at the $LaTiO_3/LaFeO_3$ interface. *Phys. Rev. B* **104**, 085115 (2021).
20. G. Araizi-Kanoutas, J. Geessinck, N. Gauquelin, S. Smit, X. H. Verbeek, S. K. Mishra, P. Bencok, C. Schlueter, T.-L. Lee, D. Krishnan, J. Fatermans, J. Verbeeck, G. Rijnders, G. Koster, M. S. Golden, Co valence transformation in isopolar $LaCoO_3/LaTiO_3$ perovskite heterostructures via interfacial engineering. *Phys. Rev. Materials* **4**, 026001 (2020).
21. M. Meng, Y. Sun, Y. Li, Q. An, Z. Wang, Z. Lin, F. Yang, X. Zhu, P. Gao, J. Guo, Three dimensional band-filling control of complex oxides triggered by interfacial electron transfer. *Nat. Commun.* **12**, 2447 (2021).
22. H. Chen, H. Park, A. J. Millis, C. A. Marianetti, Charge transfer across transition-metal oxide interfaces: Emergent conductance and electronic structure. *Phys. Rev. B* **90**, 245138 (2014).
23. Y. Cao, X. Liu, M. Kareev, D. Choudhury, S. Middey, D. Meyers, J.-W. Kim, P. J. Ryan, J. W. Freeland, J. Chakhalian, Engineered Mott ground state in a $LaTiO_{3+\delta}/LaNiO_3$ heterostructure. *Nat. Commun.* **7**, 10418 (2016).
24. J. Hoffman, I. C. Tung, B. B. Nelson-Cheeseman, M. Liu, J. W. Freeland, A. Bhattacharya, Charge transfer and interfacial magnetism in $(LaNiO_3)_n/(LaMnO_3)_2$ superlattices. *Phys. Rev. B* **88**, 144411 (2013).
25. H. Wei, J. L. Barzola-Quiquia, C. Yang, C. Patzig, T. Höche, P. Esquinazi, M. Grundmann, M. Lorenz, Charge transfer-induced magnetic exchange bias and electron localization in (111)- and (001)-oriented $LaNiO_3/LaMnO_3$ superlattices. *Appl. Phys. Lett.* **110**, 102403 (2017).
26. P. Ksoll, R. Mandal, C. Meyer, L. Schüler, V. Roddatis, V. Moshnyaga, Emergent double perovskite phase at $LaMnO_3/LaNiO_3$ interfaces: Coupled charge transfer and structural reconstruction. *Phys. Rev. B* **103**, 195120 (2021).
27. A. Tseng, A. Pham, S. C. Smith, S. Li, Tuning conductivity and magnetism in isopolar oxide superlattices via compressive and tensile strain: A case study of $SrVO_3/SrMnO_3$ and $SrCrO_3/SrMnO_3$ heterostructure. *J. Appl. Phys.* **119**, 075301 (2016).
28. S. Okamoto, J. Nichols, C. Sohn, S. Y. Kim, T. W. Noh, H. N. Lee, Charge transfer in iridate-manganite superlattices. *Nano Lett.* **17**, 2126–2130 (2017).
29. H. Chen, A. J. Millis, C. A. Marianetti, Engineering correlation effects via artificially designed oxide superlattices. *Phys. Rev. Lett.* **111**, 116403 (2013).
30. T. C. Asmara, R. J. Green, A. Suter, Y. Wei, W. Zhang, D. Knez, G. Harris, Y. Tseng, T. Yu, D. Betto, M. Garcia-Fernandez, S. Agrestini, Y. M. Klein, N. Kumar, C. W. Galdino, Z. Salman, T. Prokscha, M. Medarde, E. Müller, Y. Soh, N. B. Brookes, K.-J. Zhou, M. Radovic, T. Schmitt, Emergence of interfacial magnetism in strongly-correlated nickelate-titanate superlattices. *Adv. Mater.* **36**, 2310668 (2024).
31. Z. Liao, N. Gauquelin, R. J. Green, K. Müller-Caspary, I. Lobato, L. Li, S. Van Aert, J. Verbeeck, M. Huijben, M. N. Grisolia, V. Rouco, R. El Hage, J. E. Villegas, A. Mercy, M. Bibes, P. Ghosez, G. A. Sawatzky, G. Rijnders, G. Koster, Metal–insulator-transition engineering by modulation tilt-control in perovskite nickelates for room temperature optical switching. *PNAS* **115**, 9515–9520 (2018).
32. J. Chakhalian, S. Middey, Perspective—Emergent phases in rare earth nickelate heterostructure. *ECS J. Solid State Sci. Technol.* **11**, 053004 (2022).
33. B. Chen, N. Gauquelin, D. Jannis, D. M. Cunha, U. Halisdemir, C. Piamonteze, J. H. Lee, J. Belhadi, F. Eltes, S. Abel, Z. Jovanović, M. Spreitzer, J. Fompeyrine, J. Verbeeck, M. Bibes, M. Huijben, G. Rijnders, G. Koster, Strain-engineered metal-to-insulator transition and orbital polarization in nickelate superlattices integrated on silicon. *Adv. Mater.* **32**, 2004995 (2020).
34. R. Paudel, A. R. Burton, M. A. Kuroda, B. H. Farnum, R. B. Comes, Band-engineered $LaFeO_3$–$LaNiO_3$ thin film interfaces for electrocatalysis of water. *J. Vac. Sci. Technol. A* **41**, 063207 (2023).

35. Q. Che, I. C. G. van den Bosch, P. T. P. Le, M. Lazemi, E. van der Minne, Y. A. Birkhölzer, M. Nunnenkamp, M. L. J. Peerlings, O. V. Safonova, M. Nachtegaal, G. Koster, C. Baeumer, P. de Jongh, F. M. F. de Groot, In situ X-ray absorption spectroscopy of $LaFeO_3$ and $LaFeO_3/LaNiO_3$ thin films in the electrocatalytic oxygen evolution reaction. *J. Phys. Chem. C* **128**, 5515–5523 (2024).
36. L. Wang, P. Adiga, J. Zhao, W. S. Samarakoon, K. A. Stoerzinger, S. R. Spurgeon, B. E. Matthews, M. E. Bowden, P. V. Sushko, T. C. Kaspar, G. E. Sterbinsky, S. M. Heald, H. Wang, L. W. Wangoh, J. Wu, E.-J. Guo, H. Qian, J. Wang, T. Varga, S. Thevuthasan, Z. Feng, W. Yang, Y. Du, S. A. Chambers, Understanding the electronic structure evolution of epitaxial $LaNi_{1-x}Fe_xO_3$ thin films for water oxidation. *Nano Lett.* **21**, 8324–8331 (2021).
37. L. Wang, S. Ju, L. You, Y. Qi, Y. Guo, P. Ren, Y. Zhou, J. Wang, Competition between strain and dimensionality effects on the electronic phase transitions in $NdNiO_3$ films. *Sci. Rep.* **5**, 18707 (2016).
38. H. Guo, Z. W. Li, L. Zhao, Z. Hu, C. F. Chang, C.-Y. Kuo, W. Schmidt, A. Piovano, T. W. Pi, O. Sobolev, D. I. Khomskii, L. H. Tjeng, A. C. Komarek, Antiferromagnetic correlations in the metallic strongly correlated transition metal oxide $LaNiO_3$. *Nat. Commun.* **9**, 43 (2018).
39. S. J. May, J.-W. Kim, J. M. Rondinelli, E. Karapetrova, N. A. Spaldin, A. Bhattacharya, P. J. Ryan, Quantifying octahedral rotations in strained perovskite oxide films. *Phys. Rev. B* **82**, 014110 (2010).
40. X.-Z. Lu, J. M. Rondinelli, Epitaxial-strain-induced polar-to-nonpolar transitions in layered oxides. *Nat. Mater.* **15**, 951–955 (2016).
41. J. R. Petrie, V. R. Cooper, J. W. Freeland, T. L. Meyer, Z. Zhang, D. A. Lutterman, H. N. Lee, Enhanced bifunctional oxygen catalysis in strained $LaNiO_3$ perovskites. *J. Am. Chem. Soc.* **138**, 2488–2491 (2016).
42. L. Wang, K. A. Stoerzinger, L. Chang, X. Yin, Y. Li, C. S. Tang, E. Jia, M. E. Bowden, Z. Yang, A. Abdelsamie, L. You, R. Guo, J. Chen, A. Rusydi, J. Wang, S. A. Chambers, Y. Du, Strain effect on oxygen evolution reaction activity of epitaxial $NdNiO_3$ thin films. *ACS Appl. Mater. Interfaces* **11**, 12941–12947 (2019).
43. J. Hwang, Z. Feng, N. Charles, X. R. Wang, D. Lee, K. A. Stoerzinger, S. Muy, R. R. Rao, D. Lee, R. Jacobs, D. Morgan, Y. Shao-Horn, Tuning perovskite oxides by strain: Electronic structure, properties, and functions in (electro)catalysis and ferroelectricity. *Mater. Today* **31**, 100–118 (2019).
44. L. Wang, Z. Yang, X. Yin, S. D. Taylor, X. He, C. S. Tang, M. E. Bowden, J. Zhao, J. Wang, J. Liu, D. E. Perea, L. Wangoh, A. T. S. Wee, H. Zhou, S. A. Chambers, Y. Du, Spontaneous phase segregation of $Sr_2NiO_3$ and $SrNi_2O_3$ during $SrNiO_3$ heteroepitaxy. *Sci. Adv.* **7**, eabe2866 (2021).
45. S. R. Spurgeon, P. V. Sushko, S. A. Chambers, R. B. Comes, Dynamic interface rearrangement in $LaFeO_3/n$-$SrTiO_3$ heterojunctions. *Phys. Rev. Mater.* **1**, 063401 (2017).
46. W. T. Hong, K. A. Stoerzinger, B. Moritz, T. P. Devereaux, W. Yang, Y. Shao-Horn, Probing $LaMO_3$ metal and oxygen partial density of states using X-ray emission, absorption, and photoelectron spectroscopy. *J. Phys. Chem. C* **119**, 2063–2072 (2015).
47. M. V. Kante, M. L. Weber, S. Ni, I. C. G. van den Bosch, E. van der Minne, L. Heymann, L. J. Falling, N. Gauquelin, M. Tsvetanova, D. M. Cunha, G. Koster, F. Gunkel, S. Nemšák, H. Hahn, L. Velasco Estrada, C. Baeumer, A high-entropy oxide as high-activity electrocatalyst for water oxidation. *ACS Nano* **17**, 5329–5339 (2023).
48. P. Xu, W. Han, P. M. Rice, J. Jeong, M. G. Samant, K. Mohseni, H. L. Meyerheim, S. Ostanin, I. V. Maznichenko, I. Mertig, E. K. U. Gross, A. Ernst, S. S. P. Parkin, Reversible formation of 2D electron gas at the $LaFeO_3/SrTiO_3$ interface via control of oxygen vacancies. *Adv. Mater.* **29**, 1604447 (2017).
49. M. Gibert, M. Viret, A. Torres-Pardo, C. Piamonteze, P. Zubko, N. Jaouen, J.-M. Tonnerre, A. Mougin, J. Fowlie, S. Catalano, A. Gloter, O. Stéphan, J.-M. Triscone, Interfacial control of magnetic properties at $LaMnO_3/LaNiO_3$ interfaces. *Nano Lett.* **15**, 7355–7361 (2015).
50. Y.-M. Wu, Y. Eren Suyolcu, G. Kim, G. Christiani, Y. Wang, B. Keimer, G. Logvenov, P. A. van Aken, Atomic-scale tuning of the charge distribution by strain engineering in oxide heterostructures. *ACS Nano* **15**, 16228–16235 (2021).
51. C. Colliex, T. Manoubi, C. Ortiz, Electron-energy-loss-spectroscopy near-edge fine structures in the iron-oxygen system. *Phys. Rev. B* **44**, 11402–11411 (1991).
52. R. Mishra, Y.-M. Kim, Q. He, X. Huang, S. K. Kim, M. A. Susner, A. Bhattacharya, D. D. Fong, S. T. Pantelides, A. Y. Borisevich, Towards spin-polarized two-dimensional electron gas at a surface of an antiferromagnetic insulating oxide. *Phys. Rev. B* **94**, 045123 (2016).
53. X. Chen, X. Zhang, M. A. Koten, H. Chen, Z. Xiao, L. Zhang, J. E. Shield, P. A. Dowben, X. Hong, Interfacial charge engineering in ferroelectric-controlled Mott transistors. *Adv. Mater.* **29**, 1701385 (2017).
54. G. J. Omar, M. Li, X. Chi, Z. Huang, Z. S. Lim, S. Prakash, S. Zeng, C. Li, X. Yu, C. Tang, D. Song, A. Rusydi, T. Venkatesan, S. J. Pennycook, A. Ariando, Characteristic lengths of interlayer charge transfer in correlated oxide heterostructures. *Nano Lett.* **20**, 2493–2499 (2020).
55. R. Scherwitzl, S. Gariglio, M. Gabay, P. Zubko, M. Gibert, J.-M. Triscone, Metal-insulator transition in ultrathin $LaNiO_3$ films. *Phys. Rev. Lett.* **106**, 246403 (2011).
56. L. Wang, Y. Du, L. Chang, K. A. Stoerzinger, M. E. Bowden, J. Wang, S. A. Chambers, Band alignment and electrocatalytic activity at the *p-n* $La_{0.88}Sr_{0.12}FeO_3/SrTiO_3(001)$ heterojunction. *Appl. Phys. Lett.* **112**, 261601 (2018).
57. J. P. Perdew, A. Ruzsinszky, G. I. Csonka, O. A. Vydrov, G. E. Scuseria, L. A. Constantin, X. Zhou, K. Burke, Restoring the density-gradient expansion for exchange in solids and surfaces. *Phys. Rev. Lett.* **100**, 136406 (2008).
58. G. Kresse, J. Furthmüller, Efficient iterative schemes for ab initio total-energy calculations using a plane-wave basis set. *Phys. Rev. B Condens. Matter* **54**, 11169–11186 (1996).
59. P. E. Blöchl, Projector augmented-wave method. *Phys. Rev. B* **50**, 17953–17979 (1994).
60. R. Scherwitzl, P. Zubko, C. Lichtensteiger, J.-M. Triscone, Electric-field tuning of the metal-insulator transition in ultrathin films of $LaNiO_3$. *Appl. Phys. Lett.* **95**, 222114 (2009).
61. A. J. Hauser, E. Mikheev, N. E. Moreno, T. A. Cain, J. Hwang, J. Y. Zhang, S. Stemmer, Temperature-dependence of the Hall coefficient of $NdNiO_3$ thin films. *Appl. Phys. Lett.* **103**, 182105 (2013).
62. L. Wang, L. Chang, X. Yin, A. Rusydi, L. You, Y. Zhou, L. Fang, J. Wang, Localization-driven metal–Insulator transition in epitaxial hole-doped $Nd_{1-x}Sr_xNiO_3$ ultrathin films. *J. Phys. Condens. Matter* **29**, 025002 (2017).
63. J. Fowlie, M. Gibert, G. Tieri, A. Gloter, J. Íñiguez, A. Filippetti, S. Catalano, S. Gariglio, A. Schober, M. Guennou, J. Kreisel, O. Stéphan, J.-M. Triscone, Conductivity and local structure of $LaNiO_3$ thin films. *Adv. Mater.* **29**, 1605197 (2017).


**Acknowledgments:** We thank Advanced Photon Source at Argonne National Laboratory and Stanford Synchrotron Radiation Lightsource at SLAC National Accelerator Laboratory for providing the facility support. **Funding:** This work was supported by the US Department of Energy (DOE), Office of Science, Basic Energy Sciences, Division of Materials Sciences and Engineering, Synthesis and Processing Science Program, under award no. 10122. This research used resources of the National Energy Research Scientific Computing Center, a DOE Office of Science User Facility supported by the Office of Science of the U.S. Department of Energy under contract no. DE-AC02-05CH11231 using NERSC award BES-ERCAP0028636. Work at the University of Minnesota–Twin Cities (UMN) was supported primarily by the Air Force Office of Scientific Research (AFOSR) through grant nos. FA9550-21-1-0025 and FA9550-23-1-0247 with partial support from the UMN MRSEC program under award no. DMR-2011401. Part of the work was performed using instrumentation funded by AFOSR DURIP award FA9550-23-1-0085. Parts of this work were carried out at the Characterization Facility, UMN, which receives partial support from the National Science Foundation (NSF) through the MRSEC program under award no. DMR-2011401. Device fabrication was carried out at the Minnesota Nano Center, which is supported by the NSF through the National Nano Coordinated Infrastructure under award no. ECCS-2025124. We also acknowledge the Nano & Material Technology Development Program through the National Research Foundation of Korea (NRF) funded by Ministry of Science and ICT (RS-2024-00460372) **Author contributions:** L.W., S.A.C., B.J., and Y.D. conceived the study. Y.D. directed the project. L.W. deposited the thin films and SLs and conducted the in situ XPS characterizations and AFM measurements. L.W. and S.A.C. analyzed the in situ XPS results. Z.Y. and B.J. performed the in-plane transport property measurements and analyzed the results. K.P.K. conducted STEM/EELS experiments under the supervision of Y.D. and C.W. P.V.S. carried out the DFT simulations and generated the pDOS graphs. M.E.B. conducted the XRD measurements and analyzed the results in collaboration with L.W. J.W.F. and C.-T.K. conducted the XAS measurements separately. L.W., Z.Y., K.P.K., P.V.S., S.A.C., B.J., and Y.D. wrote the manuscript. All authors contributed to discussing the results, refining the manuscript, and providing critical feedback and revisions. **Competing interests:** The authors declare that they have no competing interests. **Data and materials availability:** All data needed to evaluate the conclusions in the paper are present in the paper and/or the Supplementary Materials.

Submitted 26 May 2024
Accepted 14 November 2024
Published 18 December 2024
10.1126/sciadv.adq6687